

Modeling of a square pulsed capillary discharge waveguide for interferometry measurements

B. H. P. Broks, W. Van Dijk, and J. J. A. W. van der Mullen^{a)}

*Department of Applied Physics, Eindhoven University of Technology,
P.O. Box 513, 5600 MD Eindhoven, The Netherlands*

A. J. Gonsalves, T. P. Rowlands-Rees, and S. M. Hooker

Department of Physics, University of Oxford, Clarendon Laboratory, Oxford OX1 3PU, United Kingdom

(Received 29 August 2006; accepted 18 December 2006; published online 2 February 2007)

Slow pulsed capillary discharges in round capillaries are currently under investigation for use as plasma channel laser waveguides in laser-wakefield acceleration, x-ray lasers, and higher-harmonic generation. In this study, a capillary discharge with a square cross section is presented. The electron density, which determines the laser guiding properties, can be measured by means of transverse interferometry in this device. Using a numerical model of the plasma and the capillary wall, an analysis of the discharge is made. The results predict that the square channel is capable of guiding circular laser pulses. The guiding properties are quite similar to those of a round channel with nearly the same diameter as the channel width. This suggests the results obtained by measuring the square capillary discharge are applicable for round channels as well. It was found that the wall heating was inhomogeneous, which makes the wall more susceptible to ablation. The heating of the wall changes the transverse optical pathlength in the interferometry experiments. © 2007 American Institute of Physics. [DOI: 10.1063/1.2432053]

I. INTRODUCTION

The interaction length between plasmas and high-powered lasers can be increased by optical guiding. Examples of the application of this interaction include high-harmonic generation,^{1,2} x-ray lasers,³⁻⁸ and laser-wakefield acceleration.^{7,9-12} This can be achieved by the use of plasma waveguides.

Plasma waveguides operate by creating an index of refraction profile that is highest in the center, focusing the laser beam and counteracting diffraction. This is achieved by creating a plasma with a concave density profile.¹³ To counteract ionization-induced refractive defocusing,¹⁴ the plasma that comes into contact with the laser should be fully ionized.

A few types of such waveguides exist, such as discharge-ablated waveguides,¹⁵⁻²¹ pinch plasmas,^{8,22,23} and slow capillary discharges.^{7,24-27} Our investigation focuses on the latter. This waveguide has the advantages of long device lifetime and of a long, stable guiding window.

Because the guiding properties depend directly on the electron density, accurate measurements of the electron density are very desirable. One method to measure the electron density in the plasma directly is via interferometry measurements. The electron density influences the index of refraction of the plasma and hence the optical pathlength through the plasma. This procedure has been successfully employed in longitudinal measurement of round channels.^{24,28} This method, however, is influenced by plasma efflux from the ends of the capillary. Furthermore, the signal is an integration of a large plasma volume, which might blur features.

These problems can be avoided by performing the interferometry perpendicular to the capillary wall.²⁹

This is, however, not possible in the standard capillary plasmas, which use round alumina (polycrystalline Al_2O_3) walls. For the interferometry, optically flat sapphire (monocrystalline Al_2O_3) walls are required. The fact that the walls are flat does mean the channel is no longer round, which makes a direct comparison with round channels less straightforward.

Earlier measurements of plasma waveguides in capillary discharges by means of transverse interferometry in square capillaries have been carried out by Jones *et al.*³⁰ Their measurements were carried out in a plasma in a mixture of ablated polyethylene, while the plasma in this work is created in hydrogen, which is prefilled in the capillary. Key plasma parameters such as thermal and electrical conductivity are quite different for these different plasma gases; hence, it is difficult to translate the results in Ref. 30 to the results in hydrogen-prefilled capillaries.

In this work, a theoretical analysis of a square pulsed capillary discharge waveguide is made. While the model presented is valid for a wide range of external parameters, the discussion is focused on one particular configuration, which matches an experimental configuration, facilitating a comparison. The square capillaries require a two-dimensional time-dependent non-local thermal equilibrium (non-LTE) model, which is considerably more challenging computationally than the one-dimensional model used earlier.^{27,31}

By modeling the plasma properties of the channel, we can provide a theoretical background and explanation of the measurements. Of particular interest is the extent to which the plasma in the square capillaries resembles the plasma in the round capillaries. This is an indication as to how descrip-

^{a)}Electronic mail: j.j.a.m.v.d.mullen@tue.nl

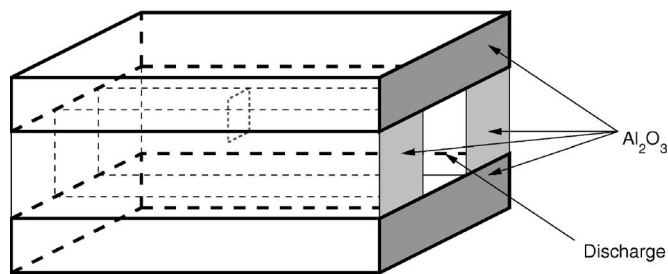


FIG. 1. A schematic drawing of the sapphire plates that constitute the capillary in which the discharge is operated. The waveguide has a length of 33 mm. The capillary that is simulated here has a width of 465 μm . The grid used to simulate the device is indicated. Due to symmetry, only a quarter of the actual area is simulated.

tive the measurements on the square channels are of plasma properties in the more common round channels. The guiding properties, i.e., the shape of an initially circular laser beam that is guided in a square waveguide and the matched spot size of the square capillary, are important in this respect.

An important practical issue is the heating of the capillary wall by the plasma. Not only may this cause ablation, but thermal expansion of the wall and the temperature dependence of the index of refraction lead to an increase in the optical pathlength through the wall. Because the transverse interferometry measurements measure the sum of the optical pathlength through plasma and wall, an increase in the latter influences the measurements and can be compensated for. The wall heating and optical pathlength increases are computed using the model, and their importance will be assessed.

In this contribution, the square pulsed capillary discharge that is the subject of the study is described in Sec. II. The model is described, emphasizing the thermal and optical wall properties, in Sec. III. The method used to obtain a matched spot size is briefly described in Sec. IV. The results of the simulation, including the plasma and guiding properties of the square channel, the thermal and optical properties of the wall, and the plasma and guiding properties of similar round channels, are presented and discussed in Sec. V. Conclusions are drawn in Sec. VI.

II. THE SYSTEM

The system consists of a square, hydrogen-filled capillary, with electrodes at either end. These are connected in parallel by a thyatron switch to a capacitor charged to 20–30 kV. By applying a current pulse, a transient hydrogen plasma is created in the capillary.

The capillary consists of two larger sapphire plates, with two smaller sapphire plates sandwiched between them in such a way that a square space is left open. It is schematically drawn in Fig. 1.

For the experiments,²⁹ capillaries of various sizes are used; in this study, a capillary with a width of 465 μm is simulated. The initial hydrogen pressure and current are also variable; in this model, an initial hydrogen pressure of 4000 Pa is used. This density is assumed constant over the length of the capillary; the construction of the capillary, in which the gas inlets are located close to its open ends, means

that this is a good assumption of the part of the capillary which lies between these inlets, but less so at the very edges. Intentional longitudinal variations of channel width¹⁶ and density^{21,30} are not the subject of this study. The current $I(t)$ is given by

$$I(t) = 600 \sin\left(\frac{\pi t}{230 \text{ ns}}\right) \text{ A}, \quad 0 \text{ ns} < t < 230 \text{ ns}, \quad (1)$$

with t the time after the beginning of a current pulse. The channel width, radius and pressure closely match an actual experimental setting,²⁹ allowing a direct comparison between experimental and theoretical results.

III. THE MODEL

The model used to simulate the square waveguide is based on the model used to simulate the round waveguide. The latter model has been discussed in great detail in Ref. 27. It has been validated by comparison with an experiment,²⁷ used for parameter studies,^{27,31} and a slightly modified version has been used to investigate the effect of modulation of the capillary radius.³² We will restrict the discussion of the model used in this work to a summary, emphasizing the difference between the present model and the model used for earlier studies, and refer the interested reader to Ref. 27 for details.

The capillary discharge waveguide consists of two separate parts: a plasma and a capillary wall. These two parts are simulated with different models and coupled via boundary conditions, allowing for a self-consistent solution of the whole system.

The plasma model is a two-dimensional two-temperature non-LTE fluid model. The bulk fluid movement is obtained from the Navier-Stokes equations:

$$\frac{\partial \rho}{\partial t} + \nabla \cdot (\rho \mathbf{v}) = 0, \quad (2)$$

$$\frac{\partial \rho \mathbf{v}}{\partial t} + \nabla \cdot (\rho \mathbf{v} \mathbf{v}) = -\nabla p + \mathbf{F}_{\text{Lor}} - \nabla \cdot (\mu \nabla \mathbf{v}). \quad (3)$$

Here, ρ is the bulk density, t is the time, \mathbf{v} is the bulk velocity, p is the bulk pressure, \mathbf{F}_{Lor} is the Lorentz force, and μ is the viscosity.

The non-LTE treatment allows for deviations of chemical equilibrium; hence, the particle conservation equations for the species that are included in the model, namely, H, H₂, H⁺, and e, have to be solved:

$$\frac{\partial n_i}{\partial t} + \nabla \cdot (n_i \mathbf{v}) = S_i. \quad (4)$$

Here, n_i is the density of species i , and S_i is the source term from chemical reactions. The chemical reactions that are included in the model are detailed in Ref. 27.

The non-LTE model separately tracks the temperature of the electrons and the heavy particles, which may differ considerably. The electron energy equation is given by

$$\begin{aligned} \frac{\partial C_e T_e}{\partial t} + \nabla \cdot [(C_e T_e + p_e) \mathbf{v}] - \mathbf{v} \cdot \nabla p_e - \nabla \cdot (\lambda_e \nabla T_e) \\ = -k_{\text{heat}}(T_e - T_h) + \frac{J^2}{\sigma} - S_e. \end{aligned} \quad (5)$$

Here, C_e is the electron heat capacity, T_e is the electron temperature, p_e is the electron pressure, λ_e is the electron heat conductivity, k_{heat} is elastic electron-heavy particle heat transfer rate, T_h is the heavy particle temperature, J is the current density, σ is the conductivity, and S_e electron energy source terms due to chemical reactions. It is noted that for the formation of the channel, λ_e was found to be of particular importance.²⁷ λ_e is computed using the Frost mixture rules,³³ which for the highly ionized plasma in the center of the discharge reduce to

$$\lambda_e \propto Z^{-2} T_e^{3/2} \quad (6)$$

with Z the ionization degree. The temperature equation for the heavy particles is given by

$$\begin{aligned} \frac{\partial C_h T_h}{\partial t} + \nabla \cdot [(C_h T_h + p_h) \mathbf{v}] - \mathbf{v} \cdot \nabla p_h - \nabla \cdot (\lambda_h \nabla T_h) \\ + \bar{\tau} : \nabla \mathbf{v} = k_{\text{heat}}(T_e - T_h). \end{aligned} \quad (7)$$

Here, C_h is the heavy particle heat capacity, p_h is the heavy particle pressure, λ_h is the heavy particle heat conductivity, and $\bar{\tau}$ is the viscosity tensor.

The model of the wall consists of a one-dimensional description of the heat transport into the sapphire wall for each point that is on the plasma/wall interface, allowing for a detailed description of the spatial and temporal variations of the wall temperature. Because the plasma and wall model are coupled via the boundary conditions, the wall temperature in turn affects the plasma behavior.

The sapphire wall is heated by the heavy particles in the plasma. This heating is computed by means of a one-dimensional heat transport equation of the sapphire wall for each point that is on the plasma-wall interface:

$$\frac{\partial C_{\text{wall}} T_{\text{wall}}}{\partial t} - \nabla \cdot (\lambda_{\text{wall}} \nabla T_{\text{wall}}) = 0, \quad (8)$$

where C_{wall} is the heat capacity of the wall material per cubic meter, T_{wall} is the wall temperature and λ_{wall} is the thermal conductivity.

The transport properties of the sapphire wall of the channel currently under study differ from the transport properties of the alumina walls of the capillaries described in our earlier studies.^{27,31} There is no significant difference in C_{wall} , which is given for both alumina and sapphire walls by^{27,34,35}

$$C_w = 3n_{\text{wall}} k_B \left[\left(\frac{\theta_E}{T_{\text{wall}}} \right) \frac{\exp\left(\frac{\theta_E}{2T_{\text{wall}}}\right)}{\exp\left(\frac{\theta_E}{T}\right) - 1} \right]^2, \quad (9)$$

with $n_{\text{wall}} = 1.17 \times 10^{29} \text{ m}^{-3}$ the density of Al_2O_3 in particles per cubic meter and $\theta_E = 690 \text{ K}$ the Einstein temperature.

However, the heat conductivity of sapphire is slightly larger than that of alumina, and is approximated well by³⁶⁻³⁹

$$\lambda_{\text{wall}} = \frac{9.9 \times 10^3 \text{ K}}{T_{\text{wall}}} \text{ W m}^{-1} \text{ K}^{-1} \quad (10)$$

for the temperature range of interest.

Wall heating changes the optical pathlength through the system, which influences the measurements. There are two contributions to the increase in optical pathlength; namely, the thermal expansion of the sapphire and the increase in refractive index of the sapphire with increasing temperature. The thermal expansion coefficient of sapphire has been obtained from Ref. 40 and is equal to $5.9 \times 10^{-6} \text{ K}^{-1}$. The temperature-dependent indices of refraction n of sapphire at the laser wavelengths λ of 532 and 1064 nm that are used for the measurements are not available in literature to the best of our knowledge. Hence, we will estimate the index of refraction from the known index of refraction at room temperature at 532 and 1064 nm,³⁵ and adding extrapolated temperature-dependent terms that are measured by Tapping *et al.*⁴¹ for 633 and 799 nm. Because the temperature-dependent terms do not depend strongly on λ and because the index of refraction itself is a smooth function of λ , we expect this extrapolation to be reasonably accurate. The resulting equations for n_{532} and n_{1064} are

$$n_{532} = 1.7676 + 1.02 \times 10^{-5} T [\text{K}] + 4.7 \times 10^{-9} T [\text{K}]^2 \quad (11)$$

and

$$n_{1064} = 1.7496 + 1.10 \times 10^{-5} T [\text{K}] + 1.6 \times 10^{-9} T [\text{K}]^2. \quad (12)$$

Wall ablation has the potential to damage the optically flat sapphire surfaces. Furthermore, the oxygen and aluminum that ablate contaminate the plasma. Both effects are quite undesirable. By computing the wall temperature T_{wall} , it can be assessed whether it remains below the melting temperature of sapphire (2326 K),³⁵ which may be used to predict ablation of the walls.

Unlike the alumina walls used in the previous studies, the sapphire walls in this case are smooth and not porous. This means far less hydrogen will desorb from them. Currently, we estimate that one hydrogen molecule desorbs from each surface site, which gives a contribution of $2.93 \times 10^{23} \text{ m}^{-3}$ at a total initial hydrogen density of $n_{\text{H}_2}^i = 1.205 \times 10^{24} \text{ m}^{-3}$.

The grid at which the simulation is performed is shown in Fig. 1. Although the system exhibits an eightfold symmetry, only the fourfold symmetry is exploited to arrive at a two-dimensional non-equidistant Cartesian grid on which the plasma is described.

In order to compare the guiding properties of the new square channel with the common round channels, simulations of equivalent round channels are also run. These simulations use the same model that is presented in Ref. 27, except for the thermal properties of the wall, for which the thermal properties of sapphire are used as described in Eq. (10). Two systems are simulated: one with an area that

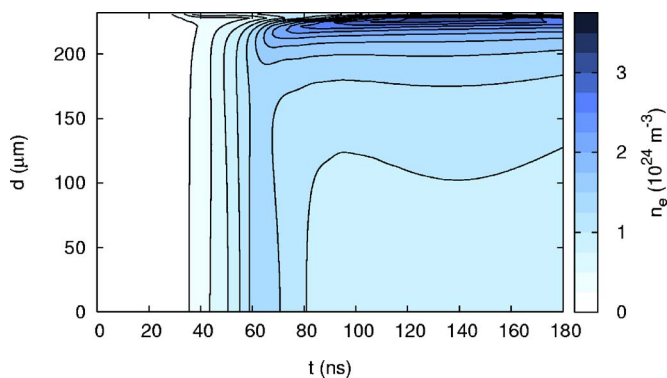


FIG. 2. (Color online) The electron density n_e as a function of time and position on a chord in the horizontal symmetry plane. The isolines indicate differences of $2.5 \times 10^{23} \text{ m}^{-3}$.

matches the area of the square channel, giving it a radius of $262 \mu\text{m}$, and one with a diameter matching the width of the square channel, giving it a radius of $232.5 \mu\text{m}$. In both cases, $n_{\text{H}_2}^i = 1.205 \times 10^{24} \text{ m}^{-3}$ and $I(t)$ is given by Eq. (1).

For the simulations, we used the PLASIMO code. This code is described in detail in Refs. 42–45. It is a modeling platform that can handle LTE and non-LTE plasmas, currently in two dimensions. Furthermore, its modular structure allows for easy expansion of the code. It has been applied to simulate a wide variety of plasma as described in Refs. 27, 31, and 46–49.

IV. LASER GUIDING THEORY

An important application of pulsed capillary discharges is the guiding of lasers. For the guiding of a Gaussian beam, a hollow, parabolic profile of the electron density n_e is optimal. Such a profile is given by

$$n_e(d) = a + \frac{1}{2}bd^2. \quad (13)$$

Here, b is the second derivative of the electron density, and a is the on-axis electron density, and d is the channel width.

The matched spot size W_m of the laser beam is given by Ref. 25:

$$W_m = (0.5\pi r_e b)^{-1/4} \quad (14)$$

with r_e the classical electron radius, which has a numerical value of $2.817 \times 10^{-15} \text{ m}$. The matched spot size can be obtained by fitting the central electron density with Eq. (13) and substituting b in Eq. (14).

The electron density is only approximately parabolic near the center of the discharge. This is not a significant issue provided the area over which n_e is parabolic is larger than the matched spot size, because such a spot size is sufficient for the bulk of the laser power to be transmitted as a Gaussian pulse.

V. RESULTS AND DISCUSSION

The square channel described in Sec. II has been simulated using the model described in Sec. III. Selected results will be presented in this section. In Sec. V A, the evolution of the plasma properties of the channel will be discussed. In

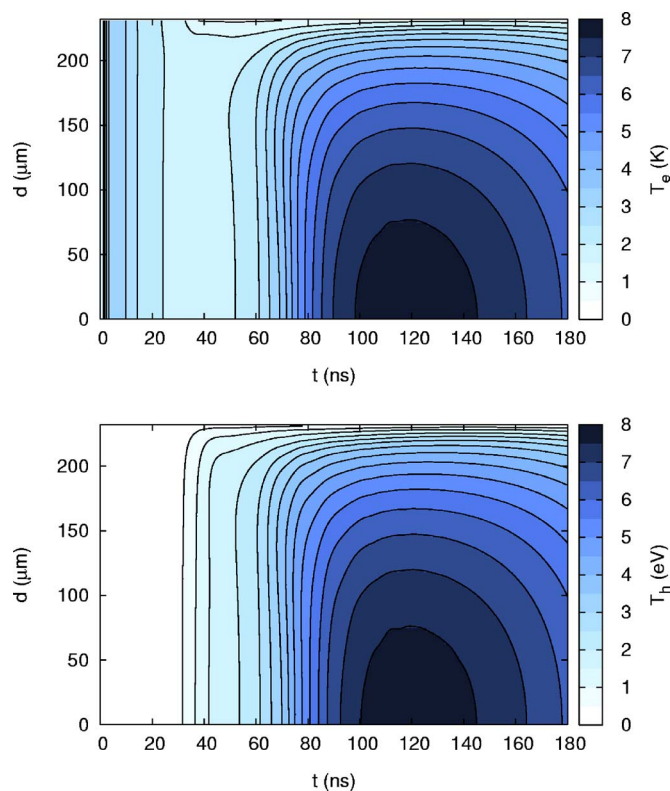


FIG. 3. (Color online) The electron temperature T_e (a) and T_h (b) as a function of time and position on a chord in the horizontal symmetry plane. The isolines indicate differences of 0.5 eV .

Sec. V B, key plasma physical parameters at the maximum of the current pulse ($t=115 \text{ ns}$) will be presented. In Sec. V C, the guiding properties will be discussed based on the n_e profiles and corresponding matched spot sizes in three different chords at $t=115 \text{ ns}$. In Sec. V D, the influence of the plasma on the capillary walls will be discussed. In Sec. V E, a comparison with round channels of equivalent radius and area will be made.

A. Evolution of the channel

The plasma channel is a strongly dynamic system, and as such, the plasma properties, including the matched spot size, vary in time. In this section, we will discuss the evolution of the plasma using three key plasma properties: the electron density n_e , the electron temperature T_e , and the heavy particle temperature T_h . These plasma properties are evaluated at a chord on the horizontal symmetry plane, for $0 \text{ ns} \leq t \leq 180 \text{ ns}$, and are presented in Figs. 2, 3(a), and 3(b), respectively. In these graphs, d denotes the position on the chord.

Qualitatively, the behavior of the channel is similar to the behavior of the round channels presented in Ref. 27. Hence, we will give only a brief description of the formation mechanism, and refer the interested reader to Ref. 27 for a more detailed discussion.

The electron temperature is initially determined by the balance between Ohmic dissipation and ionization. Because the electron density n_e increases much faster than the dissipation, the temperature drops in time. The plasma properties

are homogeneous. The heavy particle temperature starts increasing when the plasma becomes significantly ionized, approaching LTE everywhere except near the wall. The transition between these regimes is roughly around $t=50$ ns.

The increase in temperature and thermal conductivity allows significant thermal gradients to form. These thermal gradients cause a pressure gradient, which pushes the plasma to the wall, forming a hollow profile in n_e , as is seen in Fig. 2, between 60 and 100 ns. The central n_e profile is steepest near the peak of the current, at $t=115$ ns, meaning that the matched spot size is smallest at this time [cf. Eq. (14)]. After the peak of the current, the plasma slowly cools as less power is dissipated.

B. Results at the current maximum

The plasma in square channels exhibits a two dimensional structure over a cross section of the discharge. We will discuss this structure in n_e and T_e at the peak of the current, $t=115$ ns. The electron density as a function of x and y is shown in Fig. 4(a), while the electron temperature T_e as a function of x and y is shown in Fig. 4.

Figure 4(a) shows that the electron density is lowest in the center and increases towards the wall. In the corner, the n_e is again very low. Near the center, the density profile is close to being circular, as it would be in a round channel, while near the wall, the density profile is nearly square, the shape of the capillary. The consequences of this shape for the guiding properties are analyzed in Sec. IV. It is noted that a comparison of numerical results of this model with experimental results shows an excellent agreement.²⁹

The electron density profile is a result of the temperature profile, in particular T_e . T_e is so high that the plasma is fully ionized, except near the walls. Because the plasma has a nearly uniform pressure, this results in an electron density profile that is essentially the inverse of the electron temperature. This is no longer the case near the wall, and especially in the corner, as T_e is so low there that the hydrogen is no longer fully ionized.

A quantitative comparison between these results and the results in Jones *et al.*³⁰ is difficult with respect to the differences in pressure, current, and in particular the chemical composition of the plasma; our work deals with a hydrogen plasma, whereas the plasma described in their work contains hydrogen and multiply ionized carbon. One trend, however, appears to be that the carbon-hydrogen discharges have a more steeply curved parabolic profile for a given central density. Equation (6) predicts that more highly ionized plasmas have a lower thermal conductivity, and hence, for a given heat flux, higher temperature gradients. This would result in the carbon-hydrogen discharges having a steeper temperature and hence electron density profile, resulting in a smaller matched spot size, which is consistent with this work and earlier experiments.^{24,29,30} As a suggestion for further research, one could consider admixing nitrogen to the hydrogen prefilling of the capillary to increase the average ionization degree.

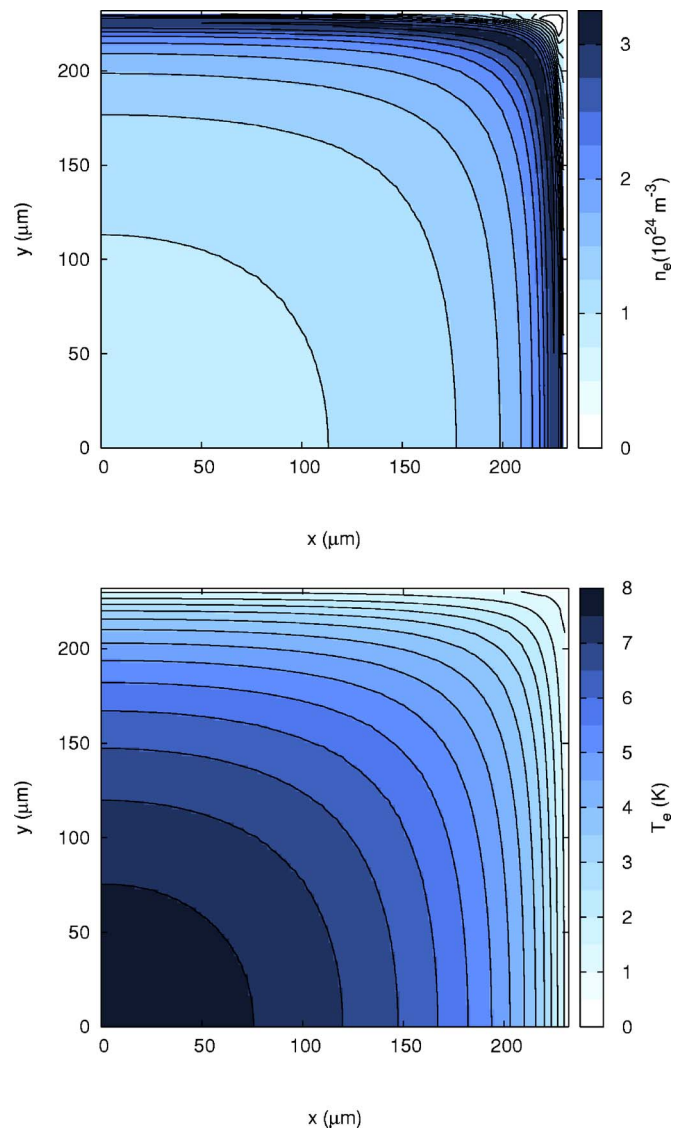


FIG. 4. (Color online) The electron density n_e (a) and electron temperature T_e over a cross section of one-quarter of the channel at $t=115$ ns.

C. Analysis of the guiding properties

In order to make a quantitative assessment of the guiding properties of the channel, the matched spot sizes at different chords through the plasma have been determined. The fit is carried out at three chords: the Horizontal chord on the horizontal symmetry plane, the Intermediate chord that passes through the axis and through the wall at three-quarters of the total width of the capillary, and the Diagonal chord on the diagonal symmetry plane, at $t=115$ ns. The electron density and fitted parabolas at these chords are presented in Fig. 5.

Near the center, the electron density profile at each chord is almost identical. The matched spot size is determined by fitting a parabola like Eq. (13) for $d < 100$ μm . Figure 5 shows that the fit is excellent in the region of interest. Using the resulting b and Eq. (14), we obtain values for the matched spots of 65.0, 65.4, and 66.0 μm for the Horizontal, Intermediate, and Diagonal chords, respectively. For a Gaussian beam, over 99% of the laser power is in the region

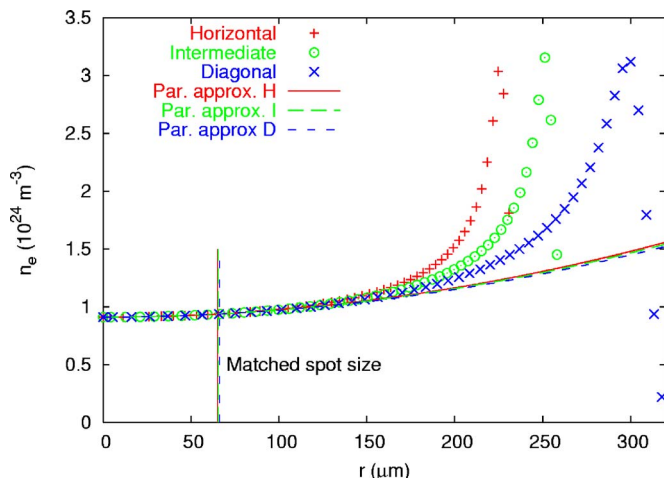


FIG. 5. (Color online) The simulated n_e and a parabolic fit through the center of the profile, at three different chords. The Horizontal chord lies in the horizontal symmetry plane, the Intermediate chord passes through the axis and through the wall at three quarters of the total width of the capillary and the Diagonal chord lies in the diagonal symmetry plane. The matched spot size at the three chords is also indicated.

covered by the parabolic fit, which means that the area over which we fit is sufficiently large to describe the behavior of the laser.

Because the matched spot size is much smaller than the fraction of the chord over which we fit, the bulk of the laser power is transmitted through this part of the channel. Hence, the we fit over a sufficiently large fraction of the chord.

The difference in matched spot size between the various chords indicates that the laser would be transmitted as a nearly circular beam: The position of isolines of the laser intensity deviates from a circular position by 0.8%.

D. Analysis of the walls

Excessive wall temperatures might lead to ablation. Because the plasma heats the wall, the hottest part of the wall is the plasma-wall interface. The temperature of this interface T_{pw} as a function of the position along the wall w and the time has been plotted in Fig. 6.

Figure 6 shows that the wall is initially heated almost homogeneously, but as the discharge progresses, the heating becomes ever more inhomogeneous, with the hottest part in the center of the wall. Furthermore, while the plasma temperature peaks near the current peak, the wall temperature continues to grow until about $t=175$ ns. The melting temperature of sapphire is not reached. Hence, ablation is not expected under these circumstances.

The wall temperature is almost homogeneous initially because the plasma temperature is as well (cf. Fig. 3). However, the plasma heats up primarily in the center, and this heat is chiefly transported via the shortest path to the wall, heating up the center of the wall more than the corners. This inhomogeneous heat load makes the wall of square capillaries more susceptible to ablation than that of round capillaries, although it is possible to prevent damage in practice. This effect is enhanced by two self-amplifying mechanisms: one in the plasma and one in the wall.

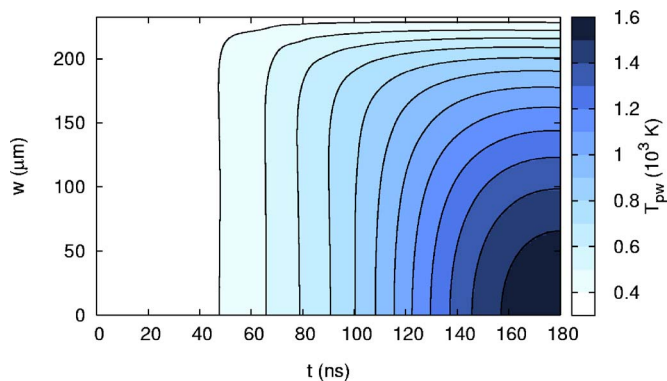


FIG. 6. (Color online) The simulated temperature at the plasma-wall interface. The corner is at $w=232.5$ μm . The isolines indicate differences of 100 K.

Throughout the plasma, apart from a small region near the wall, electron thermal conductivity is the dominant heat transport mechanism.²⁷ This transport mechanism scales with T_e^2 . Hence, hotter parts of the plasma transport more of the heat from the center to the wall, leading to inhomogeneous heating.³¹

The wall thermal conductivity scales with T_{wall}^{-1} , according to Eq. (10). This means that, when a part of the wall heats up, heat transport from this hot area is inhibited, leading to further temperature increase.

The heating of the wall induces a change in optical pathlength, both due to thermal expansion and the temperature-dependent index of refraction of the material. The increase in optical pathlength d_{opt} , for wavelengths of 532 and 1064 nm, as a function of time and position along the wall, is plotted in Fig. 7.

Quantitatively, Fig. 7 shows that the increase in optical pathlength is at most 3% of the wavelength of the light used. This is significant, but not dominant compared to the typically measured phase shifts, which are on the order of magnitude of one wavelength.²⁹ An experimental method of correcting for this different is presented in Ref. 29. The difference in optical pathlength does not depend strongly on the wavelength used. The thermal expansion and the change in index of refraction make contributions to d_{opt} that are roughly equal. Unlike T_{pw} , d_{opt} rises monotonically, which means that its influence becomes more significant as time progresses.

E. Comparison with a round channel

In order to assess to what extent the plasma and guiding properties in the square capillaries resemble those in round capillaries, we will compare selected results from the square capillaries to the results of two round capillaries with the same current and initial density, and with radii of 262 μm (channel 1) and 232.5 μm (channel 2). The former has the same area as the square capillary, while the latter has diameter equal to the width of the capillary.

The electron density, which is the plasma property that is relevant for the guiding, is presented as a function of time and radial position in Fig. 8, respectively.

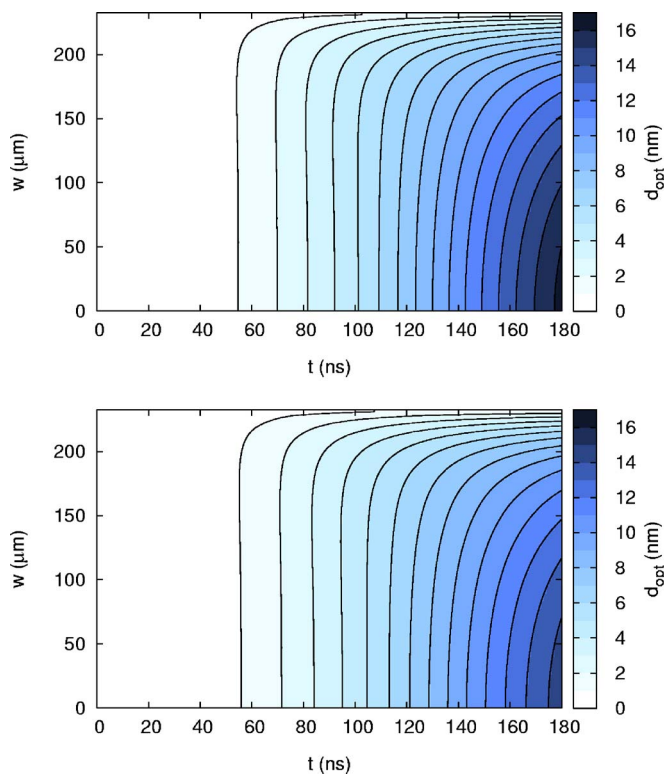


FIG. 7. (Color online) The increase in the optical pathlength through the wall due to wall heating, for a wavelength of 532 nm (a) and 1064 nm (b). The corner is at $w=232.5 \mu\text{m}$. The isolines indicate differences of $2.0 \times 10^{-9} \text{ m}$.

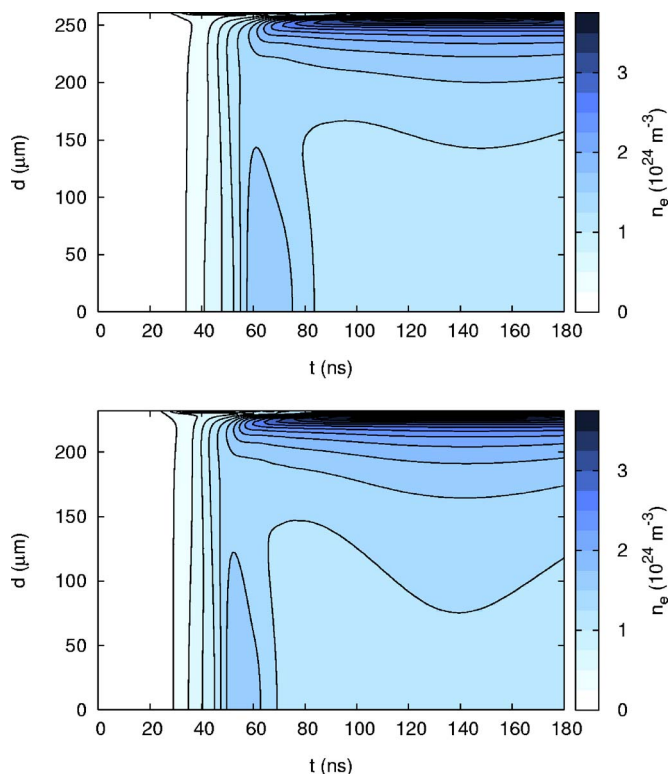


FIG. 8. (Color online) The electron density n_e as a function of time for a round channel with a radius of $262 \mu\text{m}$ (a) and $232.5 \mu\text{m}$ (b). The isolines indicate differences of $2.5 \times 10^{23} \text{ m}^{-3}$.

Comparing Figs. 2 and 8 shows that the time it takes for the plasma to ionize in the square channel is nearly the same as that in channel 1. In this stage of the discharge, the primary loss mechanism for the dissipated power is ionization, which is a local process. The dissipated power depends on the current density, which is the same in the square channel and channel 1. This means the ionization rate and hence the electron density are similar in channel 1 and in the square channel during the initial stages of the discharge.

The discharge reaches a stable, hollow profile due to heat transport to the wall. The matched spot size of channels 1 and 2 has been determined by fitting (13) to the inner $100 \mu\text{m}$ and using Eq. (14). The matched spot size for channel 1 is $69.9 \mu\text{m}$, while the matched spot size for channel 2 is $64.9 \mu\text{m}$. The matched spot size of the square channels varies between 65.0 and $66.0 \mu\text{m}$, depending on orientation. The matched spot size of the square channel lies between the matched spot size of channel 1 and channel 2, but is much closer to the matched spot size of the latter. This can be explained by noting that during the guiding phase, the heat transport properties shape the channel. These are strongly dependent on the distance that has to be traveled; because the heat transport is primarily via the path of the least thermal resistance, it is especially the shortest distance from the center to the wall that matters. This distance is identical for channel 2 and the square channel, and hence, the matched spot sizes are expected to be similar. The similarity between the guiding properties of round and square channels makes it

possible to apply scaling laws for the current, filling gas density, and channel width that have been established earlier.³¹

VI. CONCLUSION

The model presented in Ref. 27 has been successfully expanded to be able to describe two-dimensional capillary discharge waveguides with sapphire walls. This not only enables the study of square waveguides, but is also a proof of principle for the study of waveguides with other two-dimensional cross sections.

The square capillary discharge waveguide produces a plasma that has a matched spot size of $65.0 \mu\text{m}$ on a chord that lies on the horizontal symmetry axis, $65.4 \mu\text{m}$ on a chord that goes through the axis of the capillary and through the wall at three-quarters of the total height, and $66.0 \mu\text{m}$ on a chord that lies on the diagonal symmetry axis. This means a Gaussian laser pulse with a circular shape can be guided with only very little deformation of the circular shape. Both the evolution and the plasma parameters of the square channel match those of equivalent round channels closely.

The heating in the capillary wall is strongly inhomogeneous, with the highest temperatures in the center of the capillary wall. The increase in local temperature makes the wall more susceptible to ablation in comparison with round channels; however, for the setting we have studied, the temperature remained well below the ablation threshold. The heating of the capillary wall induces a change in optical

pathlength, due to the temperature dependence of the index of refraction and due to thermal expansion of the wall material.

Because the plasma and guiding properties of the square capillary discharges closely match those of the round capillary discharges, and because the temperature-induced index of refraction changes in the wall are small, the square capillary discharge is expected to be a suitable system to perform interferometry measurements on to gain insight in the electron density profile and guiding properties of capillary discharge waveguides. Furthermore, owing to the similar plasma and guiding properties, the square capillary discharge waveguide is a suitable for the same applications as a round capillary discharge waveguide.

ACKNOWLEDGMENTS

The PLASIMO team members, current and former, are acknowledged for their contributions to the code.

This work was performed as part of the research program of “Stichting voor Fundamenteel Onderzoek der Materie” (FOM) with financial support from NWO, within FOM Program 55 on Laser Wakefield Accelerators, and from EPSEC (UK) through the Basic Technology Research Programme.

- ¹H. M. Milchberg, C. G. Durfee III, and T. J. McIlrath, *Phys. Rev. Lett.* **75**, 2494 (1995).
- ²Y. Tamaki, J. Itatani, Y. Nagata, M. Obara, and K. Midorikawa, *Phys. Rev. Lett.* **82**, 1422 (1999).
- ³D. V. Korobkin, C. H. Nam, S. Suckewer, and A. Goltso, *Phys. Rev. Lett.* **77**, 5206 (1996).
- ⁴B. E. Lemoff, G. Y. Yin, C. L. Gordon III, C. P. J. Barty, and S. E. Harris, *Phys. Rev. Lett.* **74**, 1574 (1995).
- ⁵S. S. Ellwi, L. Juschkin, S. Ferri, H.-J. Kunze, K. N. Koshelev, and E. Louis, *J. Phys. D* **34**, 336 (2001).
- ⁶Z. Andreić, S. S. Ellwi, S. Pleslić, and H.-J. Kunze, *Phys. Lett. A* **335**, 430 (2005).
- ⁷D. J. Spence, A. Butler, and S. M. Hooker, *J. Opt. Soc. Am. B*, **20**, 138 (2003).
- ⁸Y. Hayashi, N. Sakamoto, Y. Zhao, Y. Cheng, P. Chalise, M. Watanabe, A. Okino, K. Horioka, and E. Hotta, *Plasma Sources Sci. Technol.* **15**, 675 (2004).
- ⁹C. Joshi and P. B. Corkum, *Phys. Today* **48**(1), 36 (1995).
- ¹⁰T. Tajima and J. M. Dawson, *Phys. Rev. Lett.* **43**, 267 (1979).
- ¹¹C. G. R. Geddes, Cs. Toth, J. van Tilborg, E. Esarey, C. B. Schroeder, D. Bruhwiler, C. Nieter, J. Cary, and W. P. Leemans, *Nature (London)* **431**, 538 (2004).
- ¹²S. P. D. Mangles, C. D. Murphy, Z. Najmudin *et al.*, *Nature (London)* **431**, 534 (2004).
- ¹³R. F. Hubbard, D. Kaganovich, B. Hafizi, C. I. Moore, P. Sprangle, A. Ting, and A. Zigler, *Phys. Rev. E* **63**, 036502 (2001).
- ¹⁴S. C. Rae, *Opt. Commun.* **97**, 25 (1993).
- ¹⁵Y. Ehrlich, C. Cohen, A. Zigler, J. Krall, P. Sprangle, and E. Esarey, *Phys. Rev. Lett.* **77**, 4186 (1996).
- ¹⁶D. Kaganovich, A. Ting, C. I. Moore, A. Zigler, H. R. Burris, Y. Ehrlich, R. Hubbard, and P. Sprangle, *Phys. Rev. E* **59**, R4769 (1999).
- ¹⁷S. M. Hooker, D. J. Spence, and R. A. Smith, *J. Opt. Soc. Am. B*, **17**, 90 (2000).
- ¹⁸M. C. Marconi, C. H. Moreno, J. J. Rocca, V. N. Shlyaptsev, and A. L. Osterheld, *Phys. Rev. E* **62**, 7209 (2000).
- ¹⁹B. Li and D. Y. Kwok, *J. Plasma Phys.* **70**, 397 (2004).
- ²⁰M. Levin, A. Pukhov, R. F. Hubbard, D. Kaganovich, D. F. Gordon, P. Sprangle, A. Ting, B. Hafizi, and A. Zigler, *Appl. Phys. Lett.* **87**, 261501 (2005).
- ²¹D. Kaganovich, A. Zigler, R. F. Hubbard, P. Sprangle, and A. Ting, *Appl. Phys. Lett.* **78**, 3175 (2001).
- ²²T. Hosokai, M. Kando, H. Dewa, H. Kotaki, S. Kondo, N. Hasegawa, K. Nakajima, and K. Horioka, *Opt. Lett.*, **25**, 10 (2000).
- ²³C. Fauser and H. Langhoff, *Appl. Phys. B: Lasers Opt.* **71**, 607 (2000).
- ²⁴D. J. Spence and S. M. Hooker, *Phys. Rev. E* **63**, 015401(R) (2001).
- ²⁵N. A. Bobrova, A. A. Esaulov, J. I. Sakai, P. V. Sasorov, D. J. Spence, A. Butler, S. M. Hooker, and S. V. Bulanov, *Phys. Rev. E* **65**, 016407 (2002).
- ²⁶A. Butler, D. J. Spence, and S. M. Hooker, *Phys. Rev. Lett.* **89**, 195003 (2002).
- ²⁷B. H. P. Broks, K. Garloff, and J. J. A. M. van der Mullen, *Phys. Rev. E* **71**, 016401 (2005).
- ²⁸D. J. Spence, P. D. S. Burnett, and S. M. Hooker, *Opt. Lett.* **24**, 993 (1999).
- ²⁹A. J. Gonsalves, T. P. Rowlands-Rees, B. H. P. Broks, J. J. A. M. van der Mullen, and S. M. Hooker, *Phys. Rev. Lett.* **98**, 025007 (2007).
- ³⁰T. G. Jones, A. Ting, D. Kaganovich, C. I. Moore, and P. Sprangle, *Phys. Plasmas* **10**, 4504 (2003).
- ³¹B. H. P. Broks, W. van Dijk, and J. J. A. M. van der Mullen, *J. Phys. D* **39**, 2377 (2006).
- ³²B. H. P. Broks, J. van Dijk, H. M. J. Bastiaens, K. J. Boller, and J. J. A. M. van der Mullen, *J. Phys. D* **39**, 2384 (2006).
- ³³L. S. Frost, *J. Appl. Phys.* **32**, 2029 (1961).
- ³⁴P. W. Atkins, *Physical Chemistry* (Oxford University Press, Oxford, 1998).
- ³⁵*CRC Handbook of Chemistry and Physics*, edited by D. R. Lide (CRC Press, Boca Raton, FL, 2004).
- ³⁶P. A. Schultz and S. A. Henion, *IEEE J. Quantum Electron.*, **27**, 1093 (1991).
- ³⁷M. G. Holland, *J. Appl. Phys.* **33**, 2910 (1962).
- ³⁸C. Kittel, *Introduction to Solid State Physics* (John Wiley & Sons, New York, 1996).
- ³⁹J. M. Ziman, *Electrons and Phonons* (Oxford University Press, Oxford, 1960).
- ⁴⁰M. Lucht, M. Lerche, H.-C. Wille, Yu. V. Shvyd'ko, H. D. Rüter, E. Gerdau, and P. Becker, *J. Appl. Crystallogr.* **36**, 1075 (2003).
- ⁴¹J. Tapping and M. L. Reilly, *J. Opt. Soc. Am. A*, **3**, 610 (1986).
- ⁴²J. van Dijk, Ph.D. thesis, Eindhoven University of Technology, 2001.
- ⁴³G. M. Janssen, Ph.D. thesis, Eindhoven University of Technology, 2000.
- ⁴⁴H. van der Heijden, Ph.D. thesis, Eindhoven University of Technology, 2002.
- ⁴⁵A. Hartgers, Ph.D. thesis, Eindhoven University of Technology, 2003.
- ⁴⁶H. van der Heijden and J. van der Mullen, *J. Phys. B* **34**, 4183 (2001).
- ⁴⁷H. van der Heijden, J. Baier, and J. van der Mullen, *J. Phys. B* **35**, 3633 (2002).
- ⁴⁸H. van der Heijden and J. van der Mullen, *J. Phys. D* **35**, 2112 (2002).
- ⁴⁹J. van Dijk, M. van der Velden, and J. van der Mullen, *J. Phys. D* **35**, 2748 (2002).